RESEARCH PAPER

Effect of synthesis conditions on local atomic structure and properties of low-toxic maghemite nanoparticles for local magnetic hyperthermia in oncology

Elena A. Kuchma [ORCID] · P. V. Zolotukhin · A. A. Belanova · M. A. Soldatov ·
A. T. Kozakov · S. P. Kubrin · O. E. Polozhentsev · P. V. Medvedev ·
Alexander V. Soldatov

Abstract Low-toxic colloidal superparamagnetic iron oxide nanoparticles (SPIONS) for theranostic applications were obtained by microwave-assisted technique. Nanoparticles were synthesized by the hydrothermal method under different conditions. XANES, XRD, and XPS studies support the maghemite (γ-Fe_2O_3) atomic and electronic structure of the nanoparticles. XANES data analysis reveals that nanoparticles have the structure reminiscent of the macroscopic maghemite. Mossbauer spectroscopy supports the γ-Fe_2O_3 phase of the nanoparticles and vibration magnetometry study shows that the nanoparticles appear to be superparamagnetic. Nanoparticle shape and size were studied by TEM and DLS methods. It was shown that the nanoparticles do not exceed 20 nm. Also, the nanoparticles are found to be low-toxic and did not have significant effects on the viability of the HeLa cell culture. The obtained nanoparticles generated heat with the highest ILP value of 2.56 nHm^2/kg and can be considered potential candidates as heat mediators for local magnetic hyperthermia in oncology.

Keywords Magnetic nanoparticles · SPIONs · Maghemite · Local magnetic hyperthermia in oncology · Toxicity · ROS · Nanomedicine

Introduction

Superparamagnetic iron oxide nanoparticles (SPIONs) are important class of perspective inorganic nanomaterials attracting attention in many fields including biomedical applications (Magnetic nanoparticles: from fabrication to clinical applications 2012). One of the interesting directions of the use of SPIONs in medical practice of near future is to explore their magnetic properties simultaneously for both diagnostics (as a contrast agent in magnetic resonance imaging (MRI)) and therapy treatment (magnetic fluid hyperthermia (MFH)). These theranostic applications of SPIONs could be an important step in effective response to the challenges in cancer treatment (Atefeh Zarepour and Khosravi 2017). Combination of SPIONs with polymeric nanostructures gives rise to polymeric nanoparticles including core–shell nanoparticles, superparamagnetic

Elena A. Kuchma and Alexander V. Soldatov contributed equally to this work.

E. A. Kuchma (✉) · P. V. Zolotukhin · A. A. Belanova ·
M. A. Soldatov · O. E. Polozhentsev · P. V. Medvedev ·
A. V. Soldatov (✉)
The Smart Materials Research Institute at the Southern
Federal University, Sladkova 178, Rostov-on-Don 344090,
Russia
e-mail: elenaku4ma@yandex.ru

A. V. Soldatov
e-mail: soldatov@sfedu.ru

A. T. Kozakov · S. P. Kubrin
Research Institute of Physics, Southern Federal University,
Rostov-on-Don, Russia

polymeric micelles, and superparamagnetic polymersomes, which have strong potential for various biomedical applications, including MRI contrast agents, drug delivery, and detection of bacteria, viruses, and proteins (Yufen Xiao n.d.). The possibility to produce SPIONs with adjustable architecture and significant progresses in their design made these nanoparticles possible to carry out several functions simultaneously such real-time monitoring and imaging of the targeted area even in vivo (Justine Wallyn and Vandamme 2019). Due to their easy synthesis, low toxicity, multifunctionality, and possibility of advanced surface modification with various surfactants, SPIONs could find effective applications in many fields of medicine (Joanna Dulińska-Litewka et al. 2019). SPIONs could be the main "working horse" for the novel diagnostic method magnetic particle imaging, having an extraordinary contrast and sensitivity, but still commercially available only for small animal treatment (Nazanin Talebloo et al. 2019).

Fine details of the local atomic structure of colloidal SPIONs are the most important characteristics which determine most of the required for theranostics application properties (Elena Kuchma and Soldatov 2018). Important advanced methods for the study of local atomic structure (in addition to standard X-ray diffraction and high-resolution transmission electron microscopy) are X-ray absorption spectroscopy at synchrotron radiation facilities and Mössbauer spectroscopy (Elena Kuchma and Soldatov 2018). Combination of SPIONs with nanoparticles–radiolabels opens additional application of such combined nanoparticles in nuclear medicine (Viviana Frantellizzi et al. n.d.). To arrange a delivery of SPIONs to specific cancer tissues, it is also possible to link these nanoparticles to antibodies (Viviana Frantellizzi et al. n.d.). Combining SPIONs with small interfering RNA made it possible to develop targeted stealth magnetic siRNA nanovectors as alternative to existing human epidermal growth factor receptor-2 cancer therapies in order to achieve a maximal therapeutic effect (Bruniaux et al. 2019).

Size isolation of SPIONs, obtained by centrifugation protocol to get SPION with well-defined sizes from a polydisperse SPION starting formulation, results (according to MRI, MPI, and MFH analyses) in seriously improved imaging and hyperthermia performance for these size-isolated SPIONs as compared to the polydisperse starting mixture (Seyed Mohammadali Dadfar et al. 2020).

It was recently shown that SPIONs as a single contrast agent could be used for dual contrast cerebrovascular magnetic resonance imaging (MRI) for simultaneously monitoring macro- and microvasculature and their association with ischemic edema status in rat models of ischemic stroke (Kang et al. 2020). Administration of SPIONs before radiation therapy could enhance the therapeutic effects of radiotherapy in some cases (Jafari et al. 2020).

In contrast to standard hydrothermal high-temperature synthesis methods, the facile low-temperature co-precipitation process without inert atmosphere could be realized by using microwave-assisted technique (Namita Saxena et al. 2020). Applying this method, low-toxic SPIONs for theranostic applications in oncology having spherical shape and maghemite structure were produced at a rate at least one order of magnitude faster than in traditional hydrothermal approach (Kuchma et al. 2017). By doping SPIONs by rare-earth atoms and by changing the synthesis conditions, one could tune the magnetic characteristics of the resulting nanoparticles. To control carefully the local structure parameters of SPIONs, one needs to combine several methods including the rather challenging but giving important information X-ray absorption near edge structure (XANES) method (Soldatov 2018). Advanced theoretical analysis of these spectra could give insight into small variation of local atomic structure parameters (Della Longa et al. 1998).

Recently, reduced graphene oxide–superparamagnetic iron oxide nanoparticle hybrids present good stability in human serum and cell viability at 24 h with GL261 and J774 cell lines and show to be rather effective T2-weighted MRI contrast agents (Marina Llenas et al. 2019).

When analyzing a biocompatibility of the SPIONs, it is interesting to study the blood compatibility as well, which is sensitive to both size (and shape) on the one hand and the type of the surfactant of the surface of nanoparticles on the other hand (Tao Liu et al. 2020). While the use of SPIONs for theranostics is going to seriously enhance the coincident diagnosis and local therapeutic applications, two important issues need to be considered when selecting SPIONs for in vivo applications: First, possible side effects and the fate of the SPIONs, i.e., elimination route or retention time in the body system if they are biodegradable (Roghayyeh Vakili-Ghartavol et al. 2020). It was also found that SPION administration to the body could result in macrophage autophagy

and induced inflammatory responses in macrophages (Rongrong Jin et al. 2019). This provides unique and novel perspectives in optimizing imaging/therapy nanoparticle performance in addition to analysis by traditional biochemical evaluation methods. In addition to treat cancer tissues themselves, SPIONs associated with alternating current magnetic field were shown to induce apoptosis of human cancer–associated fibroblasts (Ferraz 2020).

Iron oxide nanoparticles are an extremely multifaceted entity with their effects ranging from in vivo magnetism-induced hyperthermia (Zhang and Song 2016) and direct biochemical interference with cellular machinery (Hohnholt and Dringen 2013) to signaling-induced ROS generation and scavenging (Vogel et al. 2016), ROS detonation (Kosman 2013), and intracellular traffic deregulation (Daniel Hofmann et al. 2014). All these properties are of immense value for anti-cancer technologies, and the only challenge in this sense is the need to synthesize nanoparticles with such properties that will not interfere with each other and with other influences administered to cancer cells.

In the present paper, we present a study of low-toxic SPIONs produced by microwave-assistant synthesis, and their local atomic structure, magnetic properties, cytotoxicity, and characteristics for magnetic fluid hyperthermia.

Experimental section

Synthesis of superparamagnetic iron oxide nanoparticles

Magnetic nanoparticles were synthesized by means of the microwave-assisted co-precipitation method using the modified scheme as described elsewhere (Kuchma et al. 2017). The synthesis was carried out as follows. Synthesis of nanoparticles involves the preparation of an aqueous solution of divalent $FeSO_4 \bullet 6H_2O$ and trivalent $FeCl_3 \bullet 6H_2O$ iron salts. Next, a flask with the solution was placed in a microwave oven (Discover SP, CEM, USA). After the temperature reached 60 °C, the solution containing Na_2CO_3 dissolved in 10 mL of water was added to the reaction medium for 2 min. The reaction medium was maintained at 60 °C for an hour with continuous stirring. Then, 1.536 g of citric acid dissolved in 5 mL of water was added for 1 min and the sample was kept in the microwave for another 60 min. The precipitate was separated by centrifugation, which was then followed by multiple washing by means of distilled water and drying in a vacuum oven overnight at 40 °C. The advanced microwave-assisted co-precipitation method was used to obtain a sample which was named KEA02.

Two other samples were synthesized in a similar way, which was named KEA03 and KEA05. In the synthesis of KEA03, the amount of citric acid added dropwise was reduced by 5 times (which was 0.284 g) compared to the concentration of citric acid in the KEA02 sample, while in the synthesis of the KEA05 sample, the same amount of citric acid as in KEA02 was added dropwise twice as slowly as was added in the synthesis of the KEA02 sample (which was 2.5 min) (Table 1).

Geometry characterization

The X-ray diffraction (XRD) of the obtained sample was measured by the 2D PHASER (Bruker AXS Inc., Madison, WI, USA) using Cu Kα radiation ($\lambda = 1.54$ Å).

High-resolution transmission electron microscopy (HR-TEM) images were collected using the FEI Tecnai G2 F20 microscope (Hillsboro, OR, USA) operated at

Table 1 Differences in the synthesis of magnetic nanoparticles KEA02, KEA03, and KEA05

	$FeSO_4$*$6H_2O$, g	$FeCl_3$*$6H_2O$, g	Na_2CO_3, g	Citric acid, g	Time of citric acid administration, min
KEA02	1.112	2.16	3.392	1.536	1
KEA03				0.284	1
KEA05				1.536	2.5

200 kV accelerating voltage. Dynamic light scattering (DLS) was measured using the particle size analyzer NANO-flex (Microtrac, PA, USA). ζ-potential measurements were conducted using the Microtrac Stabino Particle Charge analyzer (Microtrac, PA, USA).

Using the vibration magnetometer VSM 7404 (LakeShore, USA), we measured magnetic hysteresis loops of the synthesized nanoparticles. The powder samples were measured by applied magnetic field, up to 20 Oe, at the temperature 295 K.

The Mössbauer spectra were taken with the MS1104Em spectrometer designed and built in Scientific Research Institute of Physics, Southern Federal University. The moving-source geometry was employed. The γ-ray source was ^{57}Co in a Rh matrix. The isomer shifts were calculated with respect to the metallic α-Fe. The samples were cooled in the helium cryostat CCS-850 (Janis Res. Inc., USA). The experimental spectra were fitted using SpectrRelax software (Matsnev and Rusakov n.d.).

The Fe K-edge high-energy resolution fluorescence detected (HERFD) XANES spectra were measured at ID26 beamline (Pieter Glatzela 2013) of the European synchrotron radiation facility (ESRF Grenoble, France). The measurements of frozen aqueous solutions of iron oxide magnetic nanoparticles were performed at 20 K using a helium cryostat and using a new point on the sample for each scan to minimize the radiation damage. Cryogenically cooled fixed-exit double-crystal monochromator Si (311) with an energy resolution $\Delta E/E = 0.3 \times 10^{-4}$ was used to obtain monochromatic X-ray beam. To collect HERFD XANES and XES spectra, we used an emission spectrometer equipped with four spherically bent analyzer Ge (440) crystals. The Fe K-edge HERFD XANES spectrum was recorded by scanning the energy of incident photons; the emission monochromator was fixed at the maximum energy of Fe Kα_1 emission line. Standard data reduction and linear combination fit was performed in Athena. An interval -15 eV to $+25$ eV from the edge at 7126.5 eV was chosen for linear combination fit.

A thin layer of finely powdered sample was deposed on a conductive carbon tape and fixed in a standard stainless steel sample holder. The size of an X-ray focal spot on the sample's surface was 350×500 μm. The elemental composition of the sample was determined by the spectra taken at an analyzer pass energy of 150 eV, while the C1s, O1s, and Fe2p core lines were recorded with an energy of 20 eV. The spectrometer was calibrated in advance on the Ag 3d$_{5/2}$ (368.2 eV) and Au 4f$_{7/2}$ (84.0 eV) bonding energy lines derived from reference metal surfaces previously cleaned with a flow of argon ions. Absolute resolved energy interval was measured on the full width at half maximum (FWHM) of the Ag 3d$_{5/2}$ line being not worse than 0.6 eV. To remove a weak positive charge from the sample's surface, it was irradiated by 2 eV slow electrons. XPS spectra were referenced to the C1s carbon line at a binding energy of 285.0 eV. The XPS spectra were processed in Avantage software. The background subtraction was done using the Shirley method and spectral deconvolution was performed into mixed 30% Lorentzian +70% Gaussian symmetrical components.

Cell viability assay and ROS fluorescence microscopy have been done in vitro. For in vitro cytotoxicity testing and fluorescence microscopy, we used HeLa cells as the model. For the assays, the nanoparticle formulations were re-suspended in saline so as to reach the maximum possible concentration without forming a precipitate. This concentration was approximately similar for the three samples and was adjusted to 3 mg/mL. The final concentration in the assay wells was 0.3 mg/mL due to culture medium dilution limitations.

For cell viability assay, the cells were seeded in 96-well plates (SPL Life Sciences, Pocheon-si, South Korea) in the GlutaMax DMEM (Thermo Fisher Scientific, Waltham, MA, USA) supplemented with 10% of fetal bovine serum (GE Healthcare UK Ltd., Little Chalfont, UK) and 0.05 μg/mL of gentamicin (Biokhimik JSC, Saransk, Russia). The cells were kept at 37 °C and 5% CO$_2$.

The cell viability was assessed using the trypan blue exclusion assay during 2 different days: three biological replicates per day and two technical replicates per biological replicate for each nanoparticle sample. Briefly, the cells treated with the nanoparticles and control saline were detached with 0.25% trypsin–sodium ethylenediaminetetraacetate solution and mixed with an equal volume of 0.4% trypan blue (Thermo Fisher Scientific) and, after 2 min of incubation, counted in the Goryaev chamber (the chamber is analogous to the hemocytometer; MiniMed LLC, Suponevo, Russia) under the Primo Star microscope (Carl Zeiss Meditec AG, Jena, Germany). Not <300 cells were counted in each technical replicate. The statistical calculations were performed using the SPSS 22 package. On the graph, the cell viability

data are presented as mean ± SD. The data were analyzed for normality (the zero hypothesis was retained in all groups) using the Kolmogorov–Smirnov test and for statistical differences using nonparametric (Mann–Whitney criterion) and parametric analysis of variance test for cross-consistency.

To test how the nanoparticles affected cellular reactive oxygen species (ROS) productions, we used the CellROX Green and Orange reagents (Thermo Fisher Scientific). Briefly, the cells were grown on poly-lysine-covered cover slips in 24-well plates. When the cells were 40–50% confluent, the sample and vehicle were added to the respective wells (30 μL of the sample to 300 μL of the culture medium), and then, the cells were incubated for 24 h and stained according to the manufacturer's protocol. The cells were then imaged using the BX61 microscope (Olympus Corporation, Tokyo, Japan). It should be noted that the CellROX Green reagent reacts with nuclear and mitochondrial ROS, while CellROX Orange fluorescence is only activated by cytosolic ROS. It should be stressed that HeLa cells were kindly provided by Southern Scientific Center of the Russian Academy of Sciences and validated by cytogenetic (G-staining) and molecular genetic analyses.

Hyperthermia measurements were performed by using a magnetic hyperthermia setup (LocalHyper-ThermLabUnit TOR04/16 Nanomaterials, Russia) providing an alternating magnetic field (AMF) amplitude between 2 and 20 mT with a fixed frequencies of 220–300 kHz. Temperatures of a colloidal solution were recorded with a fiber-optic probe inserted into the center of each 0.33 mL sample. The AMF is generated using a solenoid. The setup provides thermal stabilization of the sample chamber inside the solenoid. All measurements were taken several times, and samples were cooled to room temperature between measurements. Colloidal solutions with a nanoparticle concentration of 6 mg/mL were prepared for all measurements. The obtained magnetic fluids were dispersed in an ultrasonic bath, transferred into special measuring cells, and placed in the experimental setup. Hyperthermia measurements are resulting in two types of experimental data: heating temperature dependency from time and SAR dependency from field magnitude. To obtain SAR dependency from magnitude, each sample was exposed in an alternating magnetic field during a period of time (25 min).

The calorimetric approach is the most commonly adapted method in evaluating the heating efficiency of MNPs. In this approach, the temperature increase in the sample is measured over a period of time as the magnetic nanoparticles (MNPs) are exposed to an AMF of a particular amplitude and frequency (Blanco-Andujar et al. 2015; Ortega and A 2013).

The heating efficiency of MNPs is usually quantified in terms of specific absorption rate (SAR, W/g of particles) and can be expressed as:

$$SAR = \frac{C}{m_{Sample}} \frac{dT}{dt}\bigg|_{t=0} \qquad (1)$$

where C is the sample specific heat capacity (J/K/mL), m_{Sample} is the concentration of MNPs (mg/mL), and dT/dt is the initial slope of the time-dependent temperature curve.

The sample specific heat capacity C can be determined as:

$$C = C_{p,d}m_d + C_{p,NP}m_{NP} \qquad (2)$$

where $C_{p,d}$ is the specific heat capacity of the dispersion medium, $C_{p,NP}$ is the specific heat capacity of MNPs, m_d is the mass of the dispersion medium, and m_{NP} is the mass of MNPs.

The SAR value depends on the frequency f and the square amplitude H^2, which makes direct comparison of reported literature values difficult owing to variations in the applied AMF. To solve this problem, the intrinsic loss power (ILP) can be calculated whereby the SAR is normalized to the AMF strength and frequency (Blanco-Andujar et al. 2015; Ortega and A 2013):

$$ILP = \frac{SAR}{fH^2} \qquad (3)$$

To calculate the initial slope of the time-dependent temperature curve dT/dt ($t=0$), an exponential fit of the experimental data $T(t)$ is used:

$$T(t) = T_{init} + \Delta T_{max}\left(1 - e^{-\frac{t}{\tau}}\right) \qquad (4)$$

where T_{init} is the initial temperature, ΔT_{max} is the temperature change in the steady state (when $t \to \infty$), and τ is the time constant of heating.

The heating rate v of the magnetic nanoparticles is determined as:

$$v = \frac{dT}{dt}\bigg|_{t=0} = \frac{\Delta T_{max}}{\tau} \qquad (5)$$

Results and discussions

The XRD profiles of the synthesized nanoparticles (KEA02, KEA03, KEA05) confirmed the presence of nanocrystalline structures with the cubic symmetry of γ-Fe_2O_3 (maghemite) (PDF Card 39–1346) and diffraction peaks (220), (311), (400), (422), (511), (440), (620), and (533). The position of these peaks indicates the formation of iron oxide with a spinel-type structure. From the full width at half maximum (FWHM) of the (311) diffraction peak, the average-sized crystallites were calculated by means of the Debye–Scherrer equation. The result of the XRD study is presented in Fig. 1.

Morphology and size distribution of nanoparticles

The statistics to calculate the mean particle size and distribution was performed from TEM image analysis. TEM micrographs exhibited monodisperse nanoparticles, except in the case of the KEA03 sample (Fig. 2). A tendency to agglomeration in the KEA03 sample could be observed, due to 5 times less stabilizer (citric acid) in the synthesis. The analysis of the size distribution of nanoparticles was taken by means of the ImageJ program. The analysis of these images

showed that the nanoparticles are almost spherical and do not exceed 20 nm in average size. The mean sizes derived from TEM were in good accord with those calculated from XRD. For biomedical applications, nanoparticles smaller than 100 nm are usually considered. Their size may be appropriate for in vivo imaging. In practical medicine, preference is given to the spherical shape of nanoparticles, since other forms are more toxic.

Also, it is worth emphasizing that when nanoparticles are transferred to water solution different degrees of agglomeration can be observed (Kuchma et al. 2017). TEM images of KEA nanoparticles show that they are still monodisperse with a narrow size distribution (Fig. 3). In order to better define the degree of agglomeration of the water-soluble particles, DLS measurements were performed. To provide DLS and zeta potential measurements, 200 mg of each sample was suspended in 10 mL of deionized water (Milli-Q, 18.2 MΩ·cm at 25 °C) by sonication in an ultrasonic bath. The sonication lasted for 10 min and resulted in a stable colloidal solution.

Particle size distribution was determined by the NANO-Flex (Microtrac, USA) particle size analyzer. An average result of 5 consecutive measurements was used to estimate particle size distribution. The

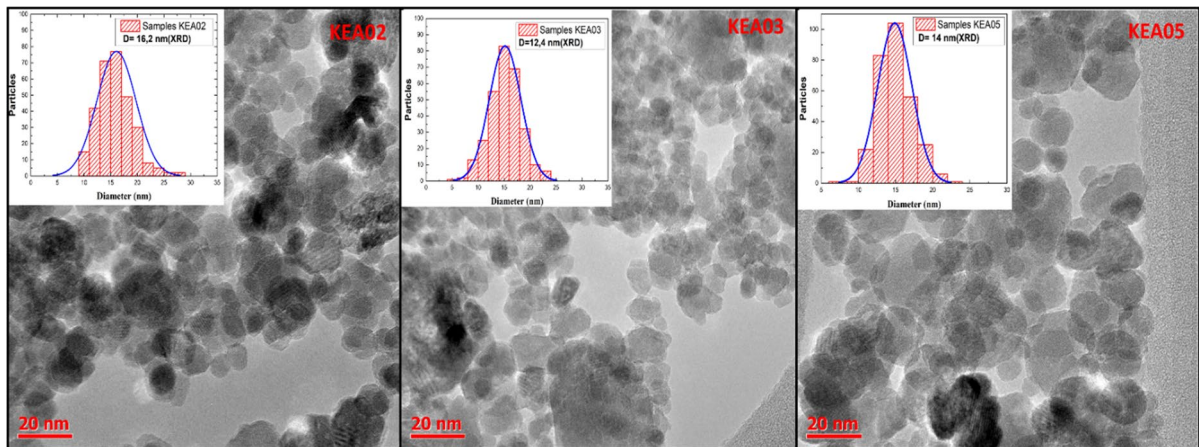**Fig. 1** X-ray diffractogram of the synthesize iron oxide nanoparticles (KEA02, KEA03, KEA05)
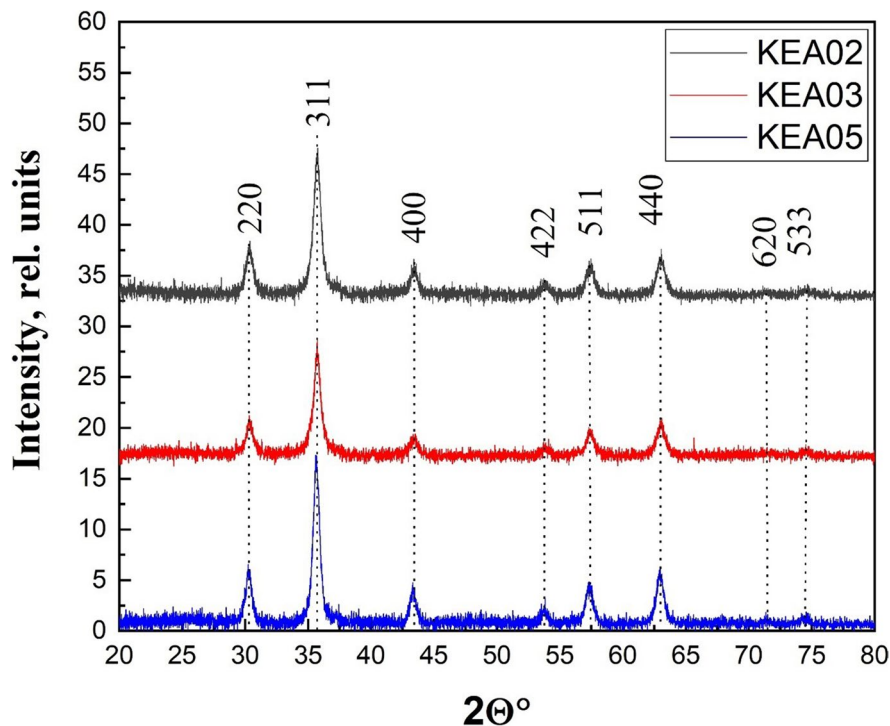
Fig. 2 TEM images and size distributions of samples (KEA02, KEA03, KEA05) synthesized using microwave-assisted co-precipitation

analysis of DLS showed that the KEA03 sample has the highest average hydrodynamic size (Dia = 77 nm). It means that the sample of KEA03 is more agglomerated than KEA02 and KEA05 samples (Fig. 3).

Simultaneous measurements of zeta potential and pH (Stabino, Particle Metrix) were performed for nanoparticles in aqueous solutions under continuous mixing. All three samples showed high negative zeta potential (−53.5 mV, −53.9 mV, and −80.8 mV for KEA02, KEA03, and KEA05, respectively) (Table 2) that is in a good agreement with the recently published zeta potential of gamma-Fe_2O_3 nanoparticles. In comparison, other iron oxides have lower modulus potential (−3 mV for Fe_3O_4 and −35 mV for FeO). Also, KEA02 and KEA05 solutions showed neutral pH, while KEA03 solution is slightly basic.

XPS

Elemental composition was performed with XPS measurements in Table 3. It is known that for solid samples, single crystals, and ceramics having surfaces processed in ultrahigh vacuum by scribing or cutting, the energy position of $Fe2p_{3/2}$ peak of iron (III) lies in the range of 711.0–711.2 eV, that of iron(II) at 710.3 eV, and in Fe_3O_4 magnetite in the range of 710.6–711.4 (Kozakov et al. 2011). Fe2p spectrum for our sample is shown in Fig. 4. Fe2p spectrum consists of two main peaks, A and D, corresponding to $2p_{3/2}$ and $2p_{1/2}$ of Fe, arising from the spin-doublet splitting of 2p level. In our case of powdered samples, the energy position of $Fe2p_{3/2}$ peak falls at 710.6 eV (Kozakov et al. 2011).

However, the energy position of $Fe2p_{3/2}$ peak cannot be the only criterion for determining the valence state of iron ions in the powdered samples, prepared under air atmosphere. As shown in Table 3, except iron lines there are also lines of carbon and oxygen present on the surface of MNPs. Deconvolution of C1s and O1s spectra into the components and their analysis show that in addition to the main peak with $E_b = 285.0$ eV (almost 60% of total content) corresponding to hydrocarbons, there are two other peaks present—one with binding energy of 286.6 eV (13.8%), corresponding to C–O, and a peak with a binding energy of 288.6 eV (25.7%), corresponding to the double bonds C=O. O1s spectra contain two components corresponding to the different iron oxides (FeO and Fe_3O_4), with binding energies of 530.1 and 531.4 eV, respectively, and two components attributed to the oxygen atoms in hydroxyl groups (OH) and water of 532.6 and 533.9 eV, respectively.

Coming back to the definition of the valence state of Fe in our samples, one can look for the presence or absence of certain characteristic features in the spectrum of iron. This feature is a component C, which is present in Fe2p spectrum of our sample (see Fig. 4). This feature is located 8.3 eV higher than $Fe2p_{3/2}$ peak, and its presence is characterized by XPS Fe2p spectrum of Fe(III) (Yamashita and P.H. 2008). This component is the so-called shake-up satellite or charge transfer satellite (CTS). In the case of Fe2p spectrum of the Fe_3O_4 sample, the
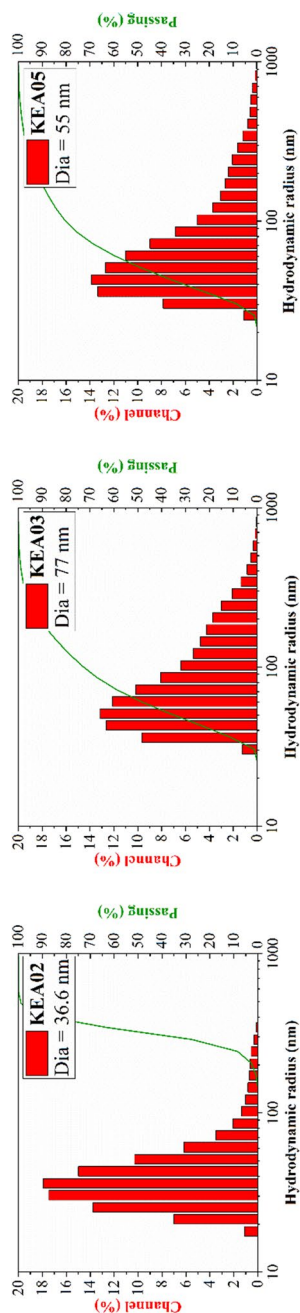
Fig. 3 The size distribution of the synthesized nanoparticles (KEA02, KEA03, KEA05) was revealed by DLS. The red columns determine the size distribution of nanoparticles; the green line is the result of fitting the spectra of the samples size distribution

Table 2 Zeta potential of the nanoparticles in aqueous solution (KEA02, KEA03, KEA05)

	Potential (ZP)	pH
KEA02	−53.5 mV	7.0
KEA03	−53.9 mV	8.7
KEA05	−80.8 mV	7.2

Table 3 Elemental composition of the MNP samples obtained by XPS

Elemental composition, atomic %		
Fe	O	C
35.7 + −2.0	50.2 + −2.7	14.1 + −1.5

charge transfer satellite is absent. The value of the relation of CTS intensity (component C) to the main peak intensity (component A) is equal 0.40 that is characterized for XPS of Fe(III). Thus, the proximity of $Fe2p_{3/2}$ energy position to the table value for Fe(III) and especially the presence of the big intensity charge transfer satellite can attribute the sample to maghemite (γ-Fe_2O_3) mainly (Yamashita and P.H. 2008). Due to the high similarities among the three samples, appearing approximately identical, we decided to report on Fig. 4 only the one referring to sample KEA02.

Magnetometry

The graphs show the hysteresis loops which characterize the dependence of magnetic moment on the applied magnetic field (Fig. 5). The maximum values of the magnetic moments of the synthesized nanoparticles are different. It is found that sample KEA02 has the highest magnetic moment to be ~67.8 emu/g. While samples KEA03 (~ 60.8 emu/g) and KEA05 (~ 65.3 emu/g) have shown lower magnetic properties than sample KEA02. Judging by the hysteresis loops, we concluded that the obtained nanoparticles appear to be superparamagnetic.

Mössbauer study

The iron oxide nanoparticles exhibit superparamagnetic properties; i.e., their magnetization vector can spontaneously reverse its orientation (Tronc and P

Fig. 4 Experimental Fe2p XPS of the obtained nanoparticle KEA02. XPS experimental spectrum shows the valence state of Fe of the obtained nanoparticle KEA02. The C satellite (dark green line) is present in the Fe_2O_3. In the case of the Fe_3O_4 sample, the C satellite is absent. The valence of samples is close to Fe_2O_3
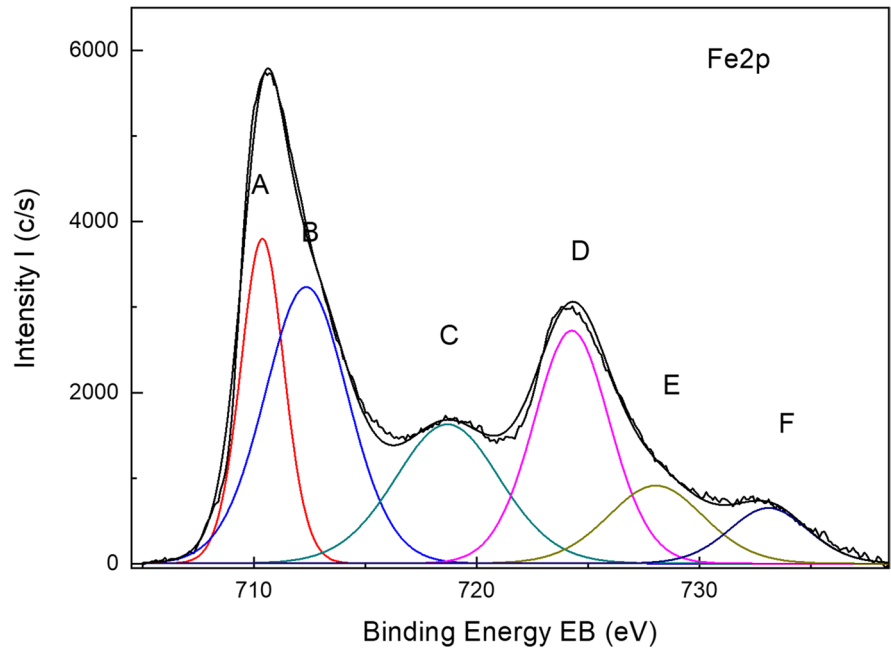
1996). The superparamagnetism leads to an asymmetric shape of the lines on the Mössbauer spectra with sharp outer and smeared inward sides (Fig. 6) (Chuev 2013). This complicates the model interpretation and reduces the reliability of the Mössbauer spectrum parameters (Soldatov 2018). To minimize the effect of the superparamagnetic relaxation, the low temperature Mössbauer study was carried out. Figure 7 shows the Mössbauer spectra of KEA iron oxide nanoparticles taken at 15 K. The Mössbauer spectra are a composition of two Zeeman sextets,

the parameters of which are listed in Table 4. The isomer shift value of the S1 sextet corresponds to the Fe^{3+} ions in octahedral coordination (Menil 1985). The isomer shift value of the S2 sextet is typical of Fe^{3+} ions in tetrahedral coordination (Menil 1985). The presence of Fe^{3+} ions in both A- and B-sites allows one to attribute the KEA samples to maghemite (γ-Fe_2O_3) (Lastovina 2018). The difference in the values of hyperfine magnetic field (*H*) correlates with the mean particle sizes. The KEA02 sample with a larger particle size has
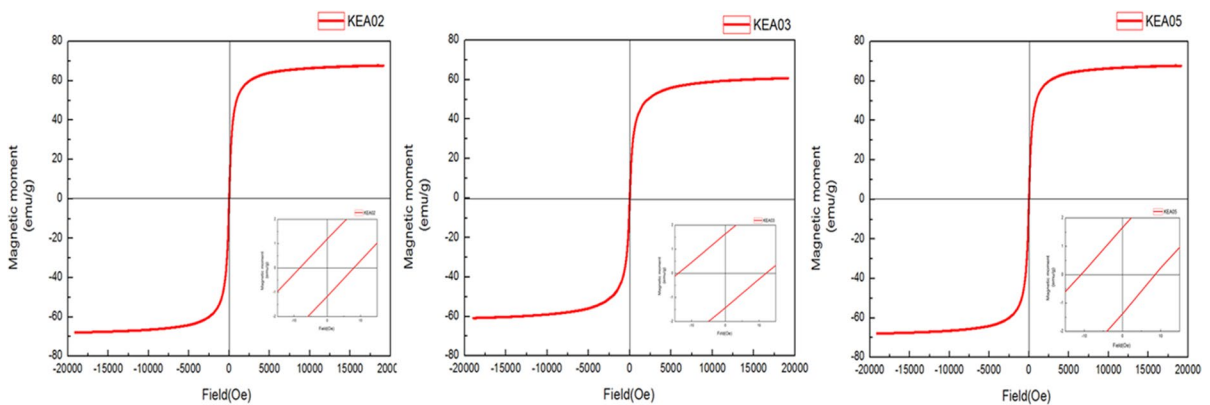

Fig. 5 Hysteresis loop which characterizes the dependence of magnetic moment on the applied magnetic field of the synthesized nanoparticles (KEA02, KEA03, KEA05)

Fig. 6 Room temperature Mössbauer spectrum of KEA nanoparticle sample. Points mark the experimental data; the black solid line is the result of fitting the spectra by distribution of hyperfine magnetic field
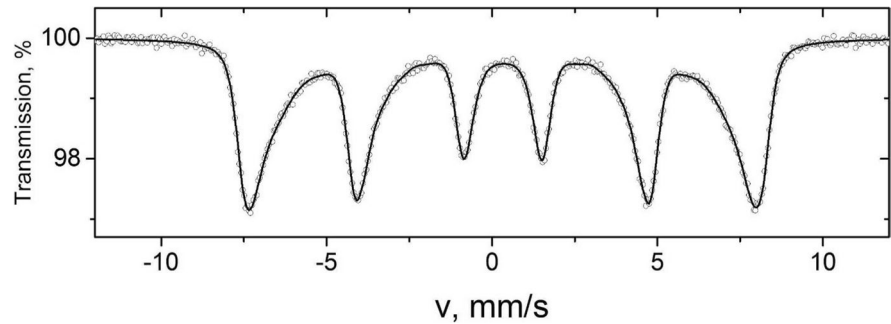
higher H values. The Mössbauer spectra of KEA samples have different values of sextet areas. This can be associated with the difference in the amount of vacancies in the B-position (Haneda 1977).

XANES study

The HERFD XANES spectra for all three samples show quite similar edge energy position and the shape of the spectra (Fig. 8) implying similar oxidation state and coordination of iron ions in the structure of nanoparticles (Soldatov 2018). A detailed view on the

rising edge energy position in comparison to the bulk magnetic phases of iron oxide shows that KEA nanoparticles have the rising edge position in between Fe_3O_4 and g-Fe_2O_3. This could be a signature of iron oxidation state to be in between that of Fe_3O_4 and g-Fe_2O_3.

Figure 9 shows that the KEA nanoparticle spectra could be reproduced at some extent with the linear combination of the spectra of bulk reference iron oxides Fe_3O_4 and g-Fe_2O_3. Particularly, KEA02 and KEA03 samples show higher content of γ-Fe_2O_3 (68.6% and 66.3%, respectively) compared to that of

Fig. 7 The Mössbauer spectra of KEA nanoparticle samples taken at 14 K. Points mark the experimental data; the black solid line is the result of fitting the spectra by sextets S1 (red shape) and S2 (blue shape); the magenta line in the bottom is a difference between fitting and experimental data. **a** KEA02. **b** KEA03. **c** KEA05
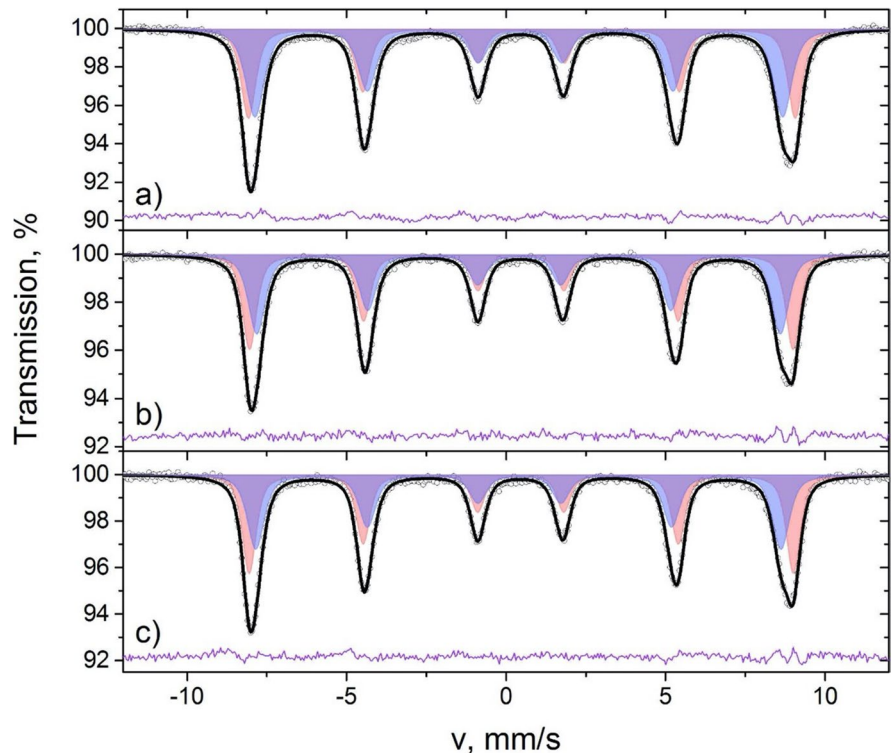
Table 4 The parameters of Mössbauer spectra of the KEA nanoparticle samples taken at 15 K

δ isomer shift, ε quadrupole shift, H hyperfine magnetic field on ^{57}Fe nucleus, A component area, G line width

Sample	Component	$\delta \pm 0.01$, mm/s	$\varepsilon \pm 0.01$, mm/s	$H \pm 0.5$, kOe	$A \pm 0.5$,%	$G \pm 0.01$, mm/s
KEA02	S1	0.48	0.01	531.8	45.0	0.56
	S2	0.42	−0.02	513.3	55.0	0.70
KEA03	S1	0.47	0.01	528.4	50.1	0.54
	S2	0.40	−0.01	509.3	49.9	0.64
KEA05	S1	0.47	0.01	529.1	52.2	0.53
	S2	0.40	−0.02	510.1	47.8	0.64

the KEA05 sample (53%) (Table 5). The latter could be a hallmark of slightly higher oxidation of KEA02 and KEA03 nanoparticles. A more detailed analysis could be used to estimate the amount of unique site positions (Soldatov et al. 2018). Taking into account the approximation that Fe_3O_4 bulk phase spectrum is formed for the contribution of iron ions in three unique site positions (Td^{3+}, Oh^{3+}, and Oh^{2+}) and γ-Fe_2O_3 in two unique site positions (Td^{3+} and Oh^{3+}), it is possible to make an estimation of the amount of iron ions of Td^{3+}, Oh^{3+}, and Oh^{2+} character (Table 5).

Cytotoxicity assay

Magnetic iron oxide nanoparticles emerge as multifunctional entities for novel diagnostics and therapy strategies in oncology (Zhao et al. 2020; Dadfar et al. 2019). In diagnostics, such nanoparticles serve as MRI contrast agents—and their properties (size, shape, charge, etc.) may be adjusted accordingly in order to perform effectively for various malignancies. Therapeutic applications are even far more versatile being well behind universal for different types of cancer, and mostly these applications require the candidate IONPs be inherently non-toxic or low-toxic. Thus, we assessed the initial toxicity of the newly synthesized KEA series nanoparticles (Fig. 10).

As seen from the results of the tests, the KEA02 and KEA03 samples had no apparent cytotoxicity in the model settings, while KEA05 exposure led to approximately 12% decrease in HeLa cell viability ($p < 0.05$). It was thus further questioned whether the three samples of the KEA nanoparticle family were dissimilar in ROS induction properties. The necessity of the testing was substantiated by the fact from our previous studies. Previously, we demonstrated that reference IONPs induced significant ROS generation while having no apparent cytotoxicity—probably due to the pattern of intracellular distribution of ROS
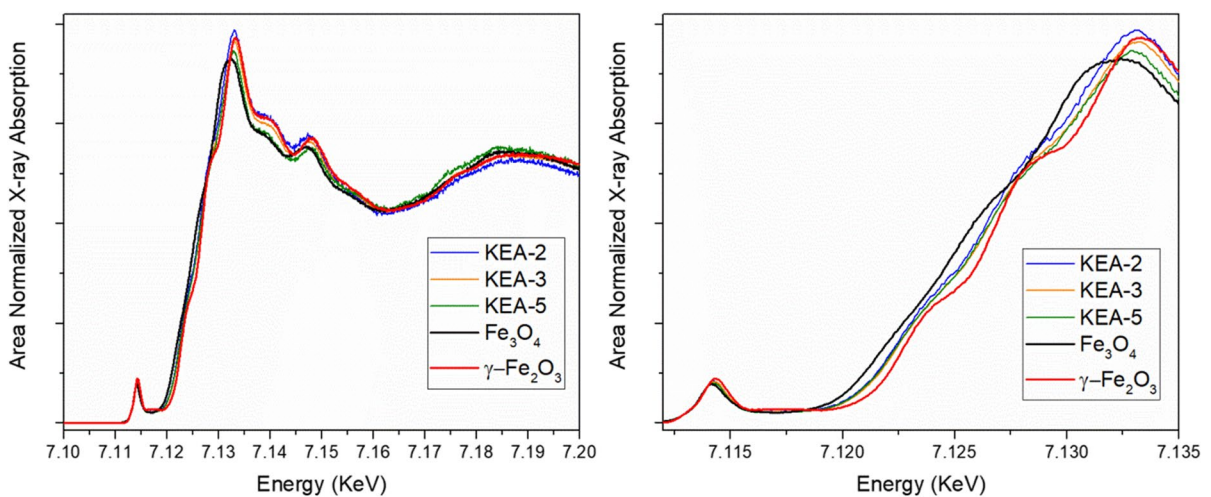

Fig. 8 a Area normalized HERFD XANES spectra for KEA nanoparticles compared to reference bulk Fe_3O_4 and g-Fe_2O_3. **b** Pre-edge feature and the rising edge of KEA nanoparticle XANES spectra compared to reference bulk Fe_3O_4 and g-Fe_2O_3
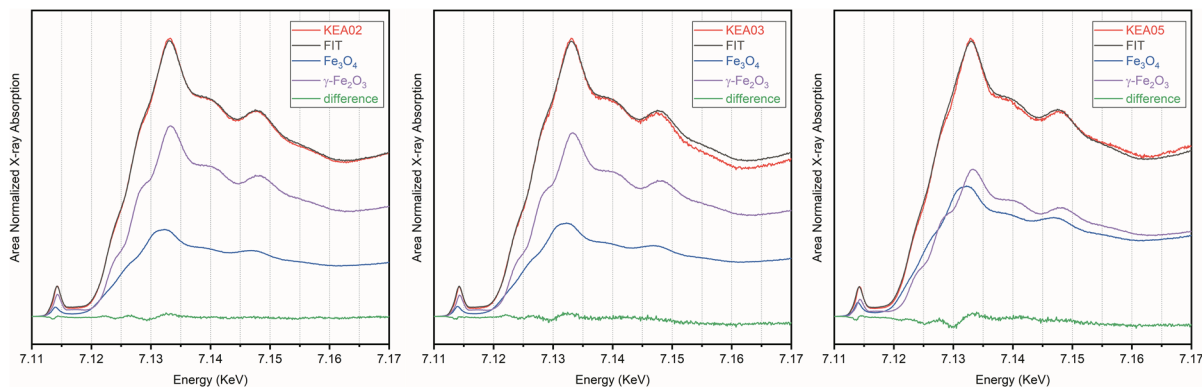
Fig. 9 The results of linear combination fit for KEA02 (**a**), KEA03 (**b**), and KEA03 (**c**) spectra with the spectra of reference Fe_3O_4 and g-Fe_2O_3 bulk compounds

Table 5 Phase and unique site composition of KEA nanoparticles

	Fe_3O_4, %	γ-Fe_2O_3, %	Td^{3+}, %	Oh^{3+}, %	Oh^{2+}, %
KEA02	31.4	68.6	44.8	44.8	10.5
KEA03	33.7	66.3	44.4	44.4	11.2
KEA05	47.0	53.0	42.2	42.2	15.7

hyper-production. In the present study, all three samples have undergone testing (Fig. 11).

As seen from Fig. 11, all three samples induced significant ROS production, and all three were absolutely distinct in their patterns of ROS generation. KEA02 induced homogenous ROS generation in the cells with cytoplasmic sources prevailing, while
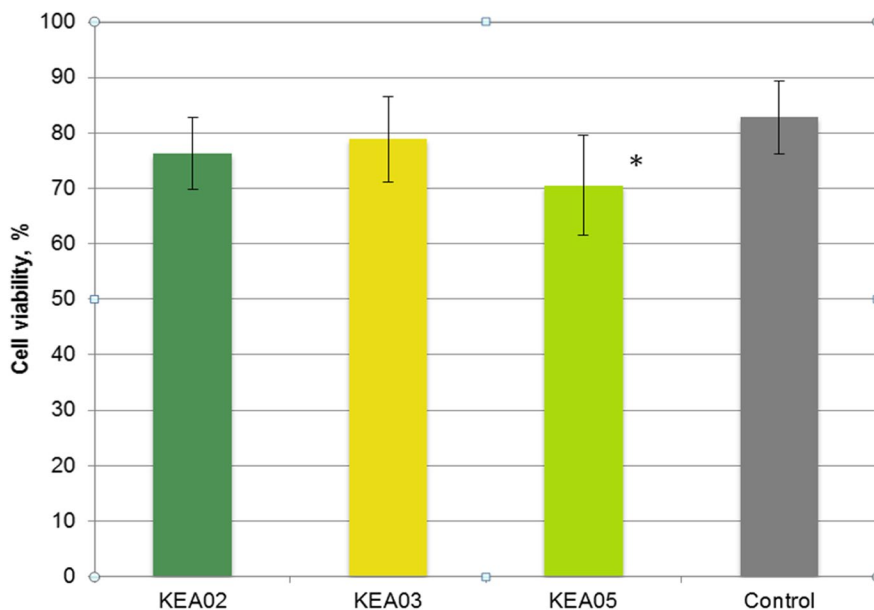

Fig. 10 Trypan blue exclusion assay results—HeLa cell viability following 24 h of exposure to 0.3 mg/mL of KEA02, KEA03, and KEA05 or vehicle. *$p < 0.05$ (KW test, ANOVA test)—cell viability significantly differs between KEA05-treated cells compared to the control group. The bars are means with error bars representing standard deviation. The fig-

ure shows the mean viability percent: KEA02 76.3%, KEA03 78.95%, and KEA05 70.5%. In comparison with the control sample (82.8%), the results of the KEA02 and KEA03 samples had no apparent cytotoxicity, while KEA05 exposure led to a 12% decrease in HeLa cell viability

KEA03 exposure resulted in mitochondria-associated ROS increase. KEA05, on the contrary, led to profound nuclear and ER ROS accumulation.

IONP application areas in oncology derive from a combination of their properties, with cytotoxicity, ROS induction, magnetism, and external magnetic field–induced oscillation heat generation being the principal determinants.

The three samples synthesized and tested in the present study differed in the first parameter, with KEA02 and KEA03 being non-toxic in the concentration tested and KEA05 demonstrating slight but statistically significant toxicity. According to the results of fluorescence microscopy, the three samples had different capabilities of inducing ROS generation. Specifically, the non-toxic samples (KEA02 and KEA03) led to increase in ROS in the compartments that were relatively well-adapted for ROS scavenging. This property is useful for combining these nanoparticles with agents targeting mitochondria or exhausting cytosolic antioxidants in the oxidative stress anti-cancer approach (Moghimi et al. 2005; Schellenberger et al. 2004).

In contrast, KEA05 mostly induced nuclear ROS. Noteworthy in this regard, nuclear antioxidant enzymes are scarce (Zolotukhin et al. 2013). In fact, copper nanoparticles used in cancer treatment mostly rely on nuclear ROS generation devastating for cancer cells (Vega-Villa et al. 2008; Wang et al. 2012). But in comparison with iron oxide nanoparticles, copper nanoparticles have significant side effects, prolonged toxicity, and even negative environmental impacts (Ingle et al. 2014). Thus, KEA05 appears to be promising substitutes for the proven effective copper nanoparticles, because while being of iron oxide nature, they possess nuclear ROS-inducing properties more like copper-based nanoparticles.

Hyperthermia

It is assumed that cancer cells are destroyed at temperatures above 42 °C, while normal cells can survive at this temperature (Ortega and A 2013; Perigo et al. 2015). Therefore, one of the ways to treat cancer is to heat locally tumor cells to a certain temperature (Deatsch and E 2014; Laurent et al. 2010; Laurent et al. 2011). This process is called hyperthermia. Thus, following this hypothesis, the next step was to determine heating characteristics of the obtained nanoparticles under the influence of an alternating magnetic field at a certain frequency and amplitude. The effect of hyperthermia strongly depends on the size of the magnetic nanoparticles. The optimum diameter for iron oxide nanoparticles is found to be

Fig. 11 ROS generation in HeLa cells after 24 h of exposure to saline (**a**) or the nanoparticle samples: KEA02 (**b**), KEA03 (**c**), or KEA05 (**d**). Dyes: CellROX green (nuclear and mitochondrial ROS) and CellROX orange (cytosolic ROS). Olympus BX-61, 600×
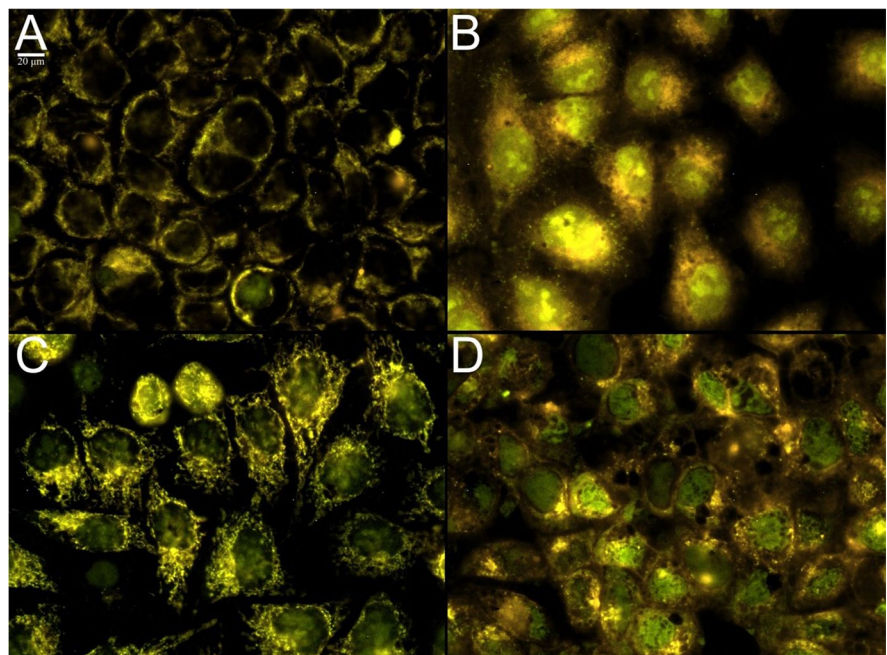
about 14 nm. The efficiency of magnetic nanoparticle hyperthermia is mainly determined by the specific absorption rate (SAR) or the intrinsic loss power (ILP) values of heat mediators that further depends on the applied magnetic field, the physicochemical and magnetic properties of nanoparticles, and the properties of the biological medium (Blanco-Andujar et al. 2015; Ortega and A 2013).

Calorimetric magnetic hyperthermia studies of all three samples were performed by measuring the time-dependent temperature rise of the aqueous ferrofluids using concentration of 6 mg/mL of the sample under exposure to AMF with different amplitudes of 2–20 mT with the step of 2 mT. All magnetic nanoparticles generated heat and heated the ferrofluids. Figure 12 shows the temperature curves of aqueous ferrofluids

of magnetic nanoparticles (KEA02, KEA03, KEA05) during a 25-min exposure of AMF with amplitudes of 10, 14, and 18 mT. The measured experimental data $T(t)$ were approximated by the exponential fit with formula (4), from which magnetic hyperthermia characteristics (SAR, ILP) were calculated with formulas (1) and (3), respectively.

All ferrofluids with a concentration of 6 mg/mL show heating to a therapeutic temperature of 42 °C under the AMF with amplitudes equal to or higher than 14 mT. The highest ILP value of 2.56 nHm^2/kg and the lowest value of 1.25 nHm^2/kg were observed for the 6 mg/mL aqueous ferrofluids of KEA05 and KEA02, respectively. Figure 12c shows the quadratic dependence of the SAR values as function of the AMF amplitude. Table 6 shows the magnetic
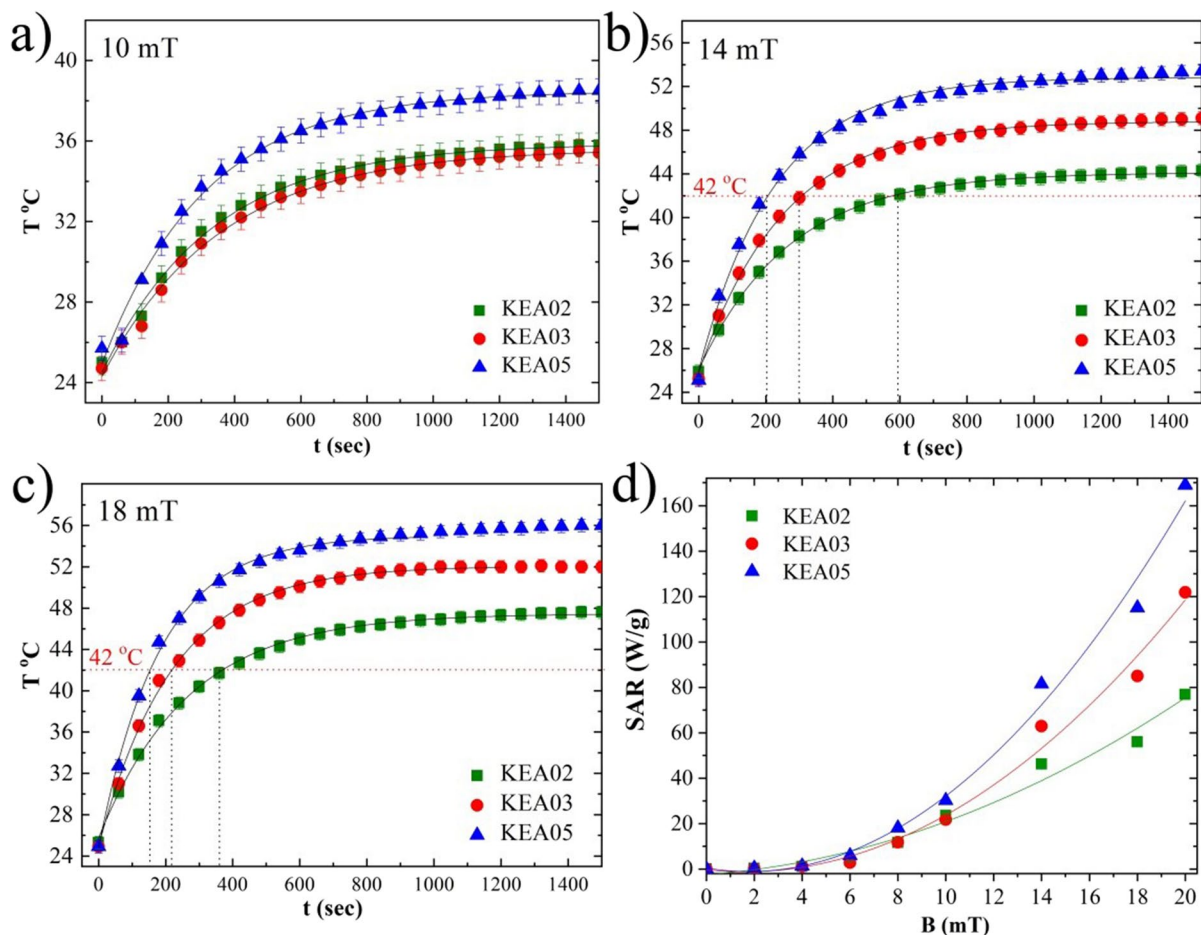

Fig. 12 a–c The time-dependent temperature curves of aqueous ferrofluids of the samples (KEA02, KEA03, KEA05) during a 25-min exposure of AMF amplitudes of 10 mT, 14 mT, and 18 mT. **d** SAR values as function of the AMF amplitude

Table 6 Magnetic hyperthermia properties obtained for all samples exposed to an alternating magnetic field (219.2 kHz, 18 mT)

Sample	SAR, W/g	ILP, nH m^2/kg
KEA02	56	1.25
KEA03	85	1.89
KEA05	115	2.56

hyperthermia properties (SAR, ILP) obtained for all samples. The obtained results are in good agreement with literature data. In general, the ILP values of SPI-ONs vary between 1 and 4 nHm^{2}kg^{-1} (Laurent et al. 2010; Laurent et al. 2011). These magnetic nanoparticles can be considered potential candidates as heat mediators for magnetic fluid hyperthermia.

Conclusions

SPIONs were prepared by means of hydrothermal microwave synthesis. As a result, nanoparticles have narrow size distribution and magnetic properties. It was found that varying the synthesis parameters leads to a change in the properties of nanoparticles and affects their behavior in cells.

The Mössbauer study revealed that iron ions appear to be in Fe^{3+} state. The Fe^{3+} ions occupy tetrahedral (A) and octahedral (B) sites. The ration of Fe^{3+} concentrations in A- and B-sites is equal to 1 only for the KEA03 sample. In KEA02 and KEA05 samples, the concentration of A-site is larger than that of B-site. This indicates that concentration of vacancies in B-position is determined by specific synthesis conditions. Thus, the method used for the synthesis of the nanoparticles under study allows one to obtain nanoparticles with various sizes and stoichiometry.

Then, the analysis of XANES spectra revealed that iron oxidation states for all nanoparticles are in between those in γ-Fe$_2$O$_3$ and Fe$_3$O$_4$. Based on the linear combination fit, it was found that KEA02 and KEA03 are more oxidized compared to KEA05.

Also, we found that nanoparticles were either non-toxic or low-toxic as tested in vitro and thus are eligible for further evaluation and development. At the same time, all three nanoformulations caused qualitative changes in cellular ROS distribution. These influences were unique for each of the formulations and

promising for compartment-targeting ROS induction, with KEA05 demonstrating an interesting copper-NP nanoparticle-mimicking properties of specific nuclear and ER ROS induction. Finally, the obtained SPIONs generated heat with the highest ILP value of 2.56 nHm^2/kg and can be considered potential candidates as heat mediators for magnetic fluid hyperthermia.

Compliance with ethical standards

Conflict of interest The authors declare no competing interests.

References

Atefeh Zarepour AZ, Khosravi A (2017) SPIONs as nano-theranostics agents. Springer

Blanco-Andujar C, Ortega D, Southern P, Pankhurst QA, Thanh NT (2015) High performance multi-core iron oxide nanoparticles for magnetic hyperthermia: microwave synthesis, and the role of core-to-core interactions. Nanoscale 7:1768–1775. https://doi.org/10.1039/c4nr06239f

Bruniaux J, A-V E, Aubrey N, Lakhrif Z, Djemaa SB, Eljack S, Marchais H, Hervé-Aubert K, Chourpa I, David S (2019) Magnetic nanocarriers for the specifc delivery of siRNA: contribution of breast cancer cells active targeting for down-regulation effciency. Int J Pharm https://doi.org/10.1016/j.ijpharm.2019.118572

Chuev MA (2013) On the shape of gammaresonance spectra of ferrimagnetic nanoparticles under conditions of metamagnetism. JETP Lett 98:465–470

Dadfar SM, Roemhild K, Drude NI, von Stillfried S, Knüchel R, Kiessling F, Lammers T (2019) Iron oxide nanoparticles: diagnostic, therapeutic and theranostic applications. Adv Drug Deliv Rev 138:302–325. https://doi.org/10.1016/j.addr.2019.01.005

Daniel Hofmann ST, Bannwarth MB, Messerschmidt C, Glaser S-F, Schild H, Landfester K, Mailander V (2014) Mass spectrometry and imaging analysis of nanoparticle-containing vesicles provide a mechanistic insight into cellular trafficking. ACS Nano 8:10077–10088

Deatsch AE, E BA (2014) Heating efficiency in magnetic nanoparticle hyperthermia. J Magn Magn Mater 354:163–172. https://doi.org/10.1016/j.jmmm.2013.11.006

Della Longa S, Pin S, Cortès R, Soldatov AV, Alpert B (1998) Fe-heme conformations in ferric myoglobin. Biophys J 75:3154–3162

Elena Kuchma SK, Soldatov A (2018) The local atomic structure of colloidal superparamagnetic iron oxide nanoparticles for theranostics in oncology. Biomedicines, 78, https://doi.org/10.3390/biomedicines6030078

Ferraz FS, L JLP, Lacerda SMSN, Procópio MS, Figueiredo AFA, Martins EMN, Guimarães PPG, Ladeira LO, Kitten GT, Dias FF, Domingues RZ, Costa GMJ (2020) Biotechnological approach to induce human fibroblast apoptosis using superparamagnetic iron oxide nanoparticles. J Inorg Biochem 206:111017

Haneda K, M AH (1977) Vacancy ordering in γ-Fe2O3 small particles 22

Hohnholt MC, Dringen R (2013) Uptake and metabolism of iron and iron oxide nanoparticles in brain astrocytes. Biochem Soc Trans 41:1588–1592. https://doi.org/10.1042/BST20130114

Ingle AP, Duran N, Rai M (2014) Bioactivity, mechanism of action, and cytotoxicity of copper-based nanoparticles: a review. Appl Microbiol Biotechnol 98:1001–1009. https://doi.org/10.1007/s00253-013-5422-8

Jafari S, M C, Tavakoli MB, Zarrabi A, Ghazikhanlu Sani K, Afzalipour R (2020) Investigation of combination effect between 6 MV X-ray radiation and polyglycerol coated superparamagnetic iron oxide nanoparticles on U87-MG cancer cells. J Biomed Phys Eng, 1

Joanna Dulińska-Litewka AŁ, Hałubiec P, Szafrański O, Karnas K, Karewicz A (2019) Superparamagnetic iron oxide nanoparticles— current and prospective medical applications. Materials, 12, https://doi.org/10.3390/ma12040617

Justine Wallyn NA, Vandamme TF (2019) Synthesis, principles, and properties of magnetite nanoparticles for in vivo imaging applications—a review. Pharmaceutics, 601, https://doi.org/10.3390/pharmaceutics11110601

Kang MungSoo, J S, Lee DK, Cho HJ (2020) MRI visualization of whole brain macro- and microvascular remodeling in a rat model of ischemic stroke: a pilot study

Kosman DJ (2013) Iron metabolism in aerobes: managing ferric iron hydrolysis and ferrous iron autoxidation. Coord Chem Rev 257:210–217. https://doi.org/10.1016/j.ccr.2012.06.030

Kozakov AT, G KA, Googlev KA, Nikolsky AV, Raevski IP, Smotrakov VG, Eremkin VV (2011) X-ray photoelectron study of the valence state of iron in iron – containing single – crystal (BiFeO3, PbFe1/2Nb1/2O3), and ceramic (BaFe1/2Nb1/2O3) multiferroics. J Electron Spectrosc Relat Phenom 184:16–23

Kuchma EA, Zolotukhin PV, Belanova AA, Soldatov MA, Lastovina TA, Kubrin SP, Nikolsky AV, Mirmikova LI, Soldatov AV (2017) Low toxic maghemite nanoparticles for theranostic applications. Int J Nanomedicine 12:6365–6371. https://doi.org/10.2147/IJN.S140368

Lastovina TA, B AP, Kubrin SP, Soldatov AV (2018) Microwave-assisted synthesis of ultra-small iron oxide nanoparticles for biomedicine. Mendeleev Commun 28:167–169

Laurent S, Bridot J-L, Elst LV, Muller RN (2010) Magnetic iron oxide nanoparticles for biomedical applications. Future Med Chem 2(3):427–449. https://doi.org/10.4155/fmc.09.164

Laurent S, Dutz S, Häfeli UO, Mahmoudi M (2011) Magnetic fluid hyperthermia: focus on superparamagnetic iron oxide nanoparticles. Adv Colloid Interf Sci 166(1–2):8–23. https://doi.org/10.1016/j.cis.2011.04.003

Magnetic nanoparticles: from fabrication to clinical applications CRC Press: Boca Raton, 2012

Marina Llenas SS, Costa PM, Oró-Solé J, Lope-Piedrafita S, Ballesteros B, Al-Jamal KT, Tobias G (2019) Microwave-assisted synthesis of SPION-reduced graphene oxide hybrids for magnetic resonance imaging (MRI). Nanomaterials 9:1364. https://doi.org/10.3390/nano9101364

Matsnev ME, Rusakov VS SpectrRelax: an application for Mössbauer spectra modeling and fitting. 178–185

Menil F (1985) Systematic trends of the 57Fe Mossbauer isomer shifts in (FeOn) and (FeFn) polyhedra. Evidence of a new correlation between the isomer shift and the inductive effect of the competing bond T-X (*Fe) (where X is O or F and T any element with a formal positive charge). J Phys Chem Solids 46:763–789

Moghimi SM, Hunter AC, Murray JC (2005) Nanomedicine: current status and future prospects. FASEB J 19(3):311–330

Namita Saxena ND, Akkireddy S, Singh A, Yadav UCS, Dube CL (2020) Efficient microwave synthesis, functionalisation and biocompatibility studies of SPION based potential nano-drug carriers. Applied Nanoscience, https://doi.org/10.1007/s13204-019-01153-8, 649–660

Nazanin Talebloo MG, Robertson N, Wang P (2019) Magnetic particle imaging: current applications in biomedical research. J Magn Reson Imagine, https://doi.org/10.1002/jmri.26875

Ortega D, A PQ (2013) Magnetic hyperthermia, in nanoscience. Nanostructures through chemistry, vol 1. Royal Society of Chemistry, Cambridge

Perigo EA, Hemery G, Sandre O, Ortega D, Garaio E, Plazaola F, Teran FJ (2015) Fundamentals and advances in magnetic hyperthermia. Appl Phys Rev 2:041302. https://doi.org/10.1063/1.4935688

Pieter Glatzela AJ (2013) X-ray absorption and emission spectroscopy. Walton, D.W.B.D.O.H.R.I., Ed

Roghayyeh Vakili-Ghartavol AAM-B, Vakili-Ghartavol Z, Aiyelabegan HT, Jaafari MR, Rezayat SM, Bidgoli SA (2020) Toxicity assessment of superparamagnetic iron oxide nanoparticles in different tissues. Artificial Cells, Nanomedicine, And Biotechnology 48:443–451

Rongrong Jin LL, Zhu W, Li D, Yang L, Duan J, Cai Z, Nie Y, Zhang Y, Gong Q, Song B, Wen L, Anderson JM, Aia H (2019) Iron oxide nanoparticles promote macrophage autophagy and inflammatory response through activation of toll-like Receptor-4 signaling. Biomaterials 203:20123–20130. https://doi.org/10.1016/j.biomaterials.2019.02.026

Schellenberger EA, Reynolds F, Weissleder R, Josephson L (2004) Surface functionalized nanoparticle library yields probes for apoptotic cells. Chembiochem 5(3):275–279

Seyed Mohammadali Dadfar DC, Darguzyte M, Roemhild K, Varvarà P, Metselaar J, Banala S, Straub M, Güvener N, Engelmann U, Slabu I, Buhl M, van Leusen J, Kögerler P, Hermanns-Sachweh B, Schulz V, Kiessling F, Lammers T (2020) Size-isolation of superparamagnetic iron oxide nanoparticles improves MRI, MPI and hyperthermia performance. J Nanobiotechnol, 18

Soldatov MA, T JG, Kubrin SP, Guda AA, Lastovina TA, Bugaev AL, Rusalev YV, Soldatov AV, Lamberti C (2018) Insight from X ray absorption spectroscopy to octahedral/tetrahedral site distribution in Sm-doped iron oxide magnetic nanoparticles. J Phys Chem:8543–8552

Soldatov MA, Gottlicher J, Kubrin SP, Guda AA, Lastovina TA, Bugaev AL, Rusalev YV, Soldatov AV, Lamberti C (2018) Insight from X-ray absorption spectroscopy to octahedral/tetrahedral site distribution in Sm-doped iron oxide magnetic nanoparticles. J Phys Chem C 122:8543–8552. https://doi.org/10.1021/acs.jpcc.7b12797

Tao Liu RB, Zhou H, Wang R, Liu J, Zhao Y, Chen C (2020) The effect of size and surface ligands of iron oxide nanoparticles on blood compatibility. RSC Adv 10:7559

Tronc EJ, P J (1996) Dispersions of γ-Fe2O3 nanoparticles. Mossbauer spectroscopic studies of the superparamagnetic relaxation. Mater Sci Forum 235-238:659–668

Vega-Villa KR, Takemoto JK, Yáñez JA, Remsberg CM, Forrest ML, Davies NM (2008) Clinical toxicities of nanocarrier systems. Adv Drug Deliv Rev 60(8):929–938

Viviana Frantellizzi MC, Pontico M, Pani A, Pani R, De Vincentis G. New frontiers in molecular imaging with superparamagnetic iron oxide nanoparticles (SPIONs): efficacy, toxicity, and future applications Nucl Med Mol Imaging

Vogel CF, Charrier JG, Wu D, McFall AS, Li W, Abid A, Kennedy IM, Anastasio C (2016) Physicochemical properties of iron oxide nanoparticles that contribute to cellular ROS-dependent signaling and acellular production of hydroxyl radical. Free Radic Res 50:1153–1164. https://doi.org/10.3109/10715762.2016.1152360

Wang Y, Zi XY, Su J, Zhang HX, Zhang XR, Zhu HY, Li JX, Yin M, Yang F, Hu YP (2012) Cuprous oxide nanoparticles selectively induce apoptosis of tumor cells. Int J Nanomedicine 7:2641–2652. https://doi.org/10.2147/IJN.S31133

Yamashita T, P.H. (2008) Analysis of XPS spectra of Fe2+ and Fe3+ ions in oxide materials. Appl Surf Sci:2441–2449

Yufen Xiao JD Superparamagnetic nanoparticles for biomedical applications. Journal of Materials Chemistry B, https://doi.org/10.1039/c9tb01955c

Zhang ZQ, Song SC (2016) Thermosensitive/superparamagnetic iron oxide nanoparticle-loaded nanocapsule hydrogels for multiple cancer hyperthermia. Biomaterials 106:13–23. https://doi.org/10.1016/j.biomaterials.2016.08.015

Zhao S, Yu X, Qian Y, Chen W, Shen J (2020) Multifunctional magnetic iron oxide nanoparticles: an advanced platform for cancer theranostics. Theranostics 10(14):6278–6309. https://doi.org/10.7150/thno.42564

Zolotukhin P, Kozlova Y, Dovzhik A, Kovalenko K, Kutsyn K, Aleksandrova A, Shkurat T (2013) Oxidative status interactome map: towards novel approaches in experiment planning, data analysis, diagnostics and therapy. Mol BioSyst 9:2085–2096. https://doi.org/10.1039/c3mb70096h